



Influence of Bulk Defect Density on the Efficiency of CIGS Based Photovoltaic Cell/Solar Cell

Mosiori, Cliff Orori ^{a*}

^a *Department of Mathematics and Physics, School of Applied and Health Sciences, Technical University of Mombasa, Box 90420 - 80100, Mombasa, Kenya.*

Author's contribution

The sole author designed, analysed, interpreted and prepared the manuscript.

Article Information

DOI: 10.56557/JOBARI/2023/v29i68577

Original Research Article

Received: 25/10/2023
Accepted: 29/12/2023
Published: 31/12/2023

ABSTRACT

In CIGS-based thin-films, bulk defects are believed to represent disturbances either in a regular, periodical arrangement within the atoms or within the crystalline media which influence sheet resistivity. In this study, first a resistivity measurements were carried out on CIGS thin films using the Van Der Pauw technique. Then, a comparison between two Van Der Pauw four-point measurement configurations (*aligned and square*) were done which showed that the square configuration was the most appropriate configuration that can be recommended to measure thin film sheet resistance of CIGS films. Finally, a numerical simulation using SCAPS-1D software was used to study the influence of bulk defect density in a CIGS films as an absorber layer in a model photocell. Using the simulated data, three operating zones for the model photocell were identified depending based on the concentration of its bulk defect density. The influence of bulk defects on thickness, band gap and doping were then analyzed. It was revealed that when the bulk defect density was less than $5 \times 10^{13} \text{ cm}^{-3}$ for an absorber of thickness in the order of over $3 \mu\text{m}$, a band gap between 1.3 eV-1.4 eV and acceptor density of 10^{16} cm^{-3} were the optimal operating conditions for the model photocell. It was concluded that the CIGS layer used as an absorber can be improved if its bulk defect density is tuned to optimal levels.

*Corresponding author: E-mail: corori@tum.ac.ke;

Keywords: Numerical simulation; bulk defect density; CIGS; absorber; acceptor density.

1. INTRODUCTION

Thin technology can be used to fabricate copper indium gallium selenide (CIGS) photovoltaic cells. These are heterojunction photo cells where the CIGS layer form the absorber layer. In this cells, the CIGS is the p-type layer and occupies the largest surface area of the photocell. It is the most important layer [1] of the cell and it is usually covered by an n-type buffer layer to provide a P-N junction interface [2]. Most of these heterojunction devices use a thin layer of CdS on top of the buffer layer with a transparent conductive oxide of a higher resistivity forming a third thin layer [3]. This complete assembly is then deposited on a recommended substrate to offer mechanical support. Most prototype CIGS photocells use the soda-lime glass substrate because of its compatability with CIGS crystals making them one of the most highly efficiency CIGS-based photovoltaic devices. For purposes of testing, two different ohmic contacts made out of either molybodium or an alloy of nickel-aluminium (Ni/Al) [4] are used to collect any photo-generated electrons and holes upon illumination. Recent studies [5, 6, 7] have successfully investigated many opto-electrical parameters of CIGS photocells but few have concentrated on the influence of bulk defect density on their performance.

A defect is considered to be shallow when its energy level is very close to the minima of a conduction band or very close to maxima of a valence band [8], otherwise it is regarded as a deep defect. Deep defects are very common in many doped materials [8, 9, 10]. They are considered to be free carrier traps known to capture charge carriers that are introduced through doping [9]. The amount of bulk defects in an absorber layer may influence the optical and electrical capabilities of many thin film photocells. These bulk defects have been classified into four categories as follows; point defects believed to be represented by vacancies [11, 12]; interstitial defects [13]; anti-site defects [14] and linear defects which correspond to dislocations in crystalline materials. All these defects can be analyzed in two different ways; two-dimensional defects (*grain boundaries*) or as three-dimensional defects [5, 12]. It is true that crystal imperfections manifest themselves as bulk defects and bulk defects in an active absorber can be regulated easily by regulating depositional conditions [15]. Bulk defects play a significant

role. One way is by influencing charge carrier transport mechanisms in lattice crystalline structures by either influencing charge generation or charge separation or electron-hole pair recombinations within the absorber [1]. That is why they act as periodic disturbances in crystalline materials having regularly arranged atoms in their crystals. It is therefore necessary to evaluate the influence of bulk defect density so that we understand how to control them or how to precisely create them [10] depending on their influence and application. The article highlights findings on the impact of bulk defect density on thickness, band gap, doping concentration and performance of CIGS photovoltaic cells.

2. THEORY

2.1 Thin Film Resistivity

To measure thin film resistivity, two configurations are recommended. One of them is the four-contact point configuration that can correct the insufficiencies of its two point configuration counterpart. In the four-contact point configuration, two points inject current while the other two points measure potential difference using the LCR meter [16]. By knowing both the injected currents and voltages at specific film thickness, resistivity or impedance can be computed using the Van der Pauw technique [3]. Its complex impedance, Z_x is then computed using:

$$Z_x = -\left(\frac{V_1}{V_2}\right)R \quad (1)$$

The aligned configuration uses a rectangular shape of length, a and width, d with four arbitrary points aligned at equal tip spacing, s on a surface arranged as $I_{Hcu}V_{Hpot}$ and $V_{Lpot}I_{Lcu}$ where I_{Hcu} and I_{Lcu} are dedicated to current injection points while V_{Hpot} and V_{Lpot} are dedicated to voltage measurement points [17]. Resistivity is then computed using Eq. (2) as:

$$\rho = \frac{V}{I} \left(\frac{d}{s}; \frac{a}{d}\right) e \times C \quad (2)$$

where ρ is resistivity, V is the measured potential difference while I is the low currents injected into the film and C is the coefficient of the correction

factor which depends on the width and distance between the configuration tip points. In a square configuration, only 4-points are arbitrary arranged on the edges and numbered from 1 to 4 to form a square. Current is injected and voltage measured so that the $R_{12,34}$ and $R_{14,23}$ resistances are used to compute resistivity from using Eq. (3) and Eq. (4) respectively:

$$e \left(\frac{-\pi e}{\rho} R_{12,34} \right) + e \left(\frac{-\pi e}{\rho} R_{14,23} \right) = 1 \quad (3)$$

$$\rho = \frac{\pi e}{\ln 2} R = \frac{\pi V e}{I \ln 2} \quad (4)$$

2.2 Thin Film Optical Properties

The CIGS band gap form an important parameter to consider when improving the performance of it's photocell [18]. It determines how photon absorption and charge carrier generation takes place [19]. When gallium (Ga) is introduced into CIS absorber to form CIGS by gallium levels between $x = 0$ and $x = 1$, its band gap widens from 1.021 eV to about 1.672 eV [3, 9]. It is a clear indicator that the introduced bulk defects influence band gap. This implies that an increase in concentration influences band gap by adjusting its conduction band minima [11]. Under a controlled deposition processes, the band gap of CIGS has been found to vary linearly with gallium concentration [7, 20] by Eq. (5) as;

$$E_g = [1.021 + 0.611x - bx(1-x)] \text{ eV} \quad (5)$$

forming a $\text{CuIn}_{1-x}\text{Ga}_x\text{Se}_2$ composite. Parameters such as absorption coefficient [3], electron affinity [7] and bulk defect density [15] are adjusted by some correction factor that can also depend on bulk defect density. The density of bulk defects is increasing becoming a key factor to consider when analysing the limits by which CIGS photocells can perform even at higher gallium concentration levels that may be above the theoretical values.

2.3 Photocell Performance

Numerical simulations can be used to study the influence of bulk defect density on the efficiency of many photocells without carrying out actual experiments. One can accurately characterize a photocell using simulations only. The SCAPS-1D is a software that use the Finite-Difference Method to solve many basic equations with well-defined boundary conditions applicable to many optical devices and they equations include:

(i) the Poisson equation [21] given by;

$$\nabla^2 \Phi = - \left(\frac{\rho}{\epsilon_0} \right) \quad (6)$$

The equation is commonly used in a region where there are no currents so that parameters, ρ and J both vanish resulting into a Laplace's equation expressed as;

$$\nabla^2 \Phi = 0 \quad (7)$$

(ii) the electron continuity equation [22] or the law of conservation of charge expressed as:

$$\frac{\partial n}{\partial t} = - \left(\frac{\partial P_n}{\partial n} \right) + gn \left(- \frac{p}{\tau_p} \right) \quad (8)$$

(iii) and the hole continuity equation [19] expressed as ;

$$\frac{\partial p}{\partial t} = - \left(\frac{\partial P_p}{\partial n} \right) + gp \left(- \frac{p}{\tau_p} \right) \quad (9)$$

where all the symbols have their usual scientific meanings. Both of the continuity equations are used to evaluate carrier concentration rates when recombination, generation, drift and diffusion process takes place simultaneously. Under normal conditions, the rate of change of charge carrier concentration is equal to the sum of drift, diffusion and charge generation less it's recombination rates [23].

3. METHODOLOGY

3.1 Materials

An argon gas source, molybdenum foil substrates, a selenium-rich gaseous source, hexanethiol and sodium fluoride solutions were among the reagents that were purchased from Sigma and Aldrich Co.

3.2 Film Deposition

A magnetron sputtering machine was used to sputter CIG on a molybdenum foil substrate with a target power density of 10 mW cm^{-2} in the presence of an argon gas flowing at a pressure of 10 mTorr at about 27°C . The thickness of the CIGS absorber film was varied by precisely controlling the repeated spin coating process and

heating in a selenium-rich environment for 15 minutes at 590° C. About 1.96 mg of sodium fluoride was mixed with a 1.55 mL of hexanethiol precursor solution to form a sodium ink doping solution. This solution was then deposited on the molybdenum-coated substrate directly by spin coating. All other film processing and procedures were carried out followed the work by Xu [1].

3.3 Characterization

3.3.1 Measurement of resistivity

Four-point measurements were repeatedly carried out using HP 4284A LCR meter with its tester in serial RL mode at short factor of correction to eliminate any residual impedance. For measurements in the aligned four point configuration, a rectangular structure with a length of “a” and “d” wide at equal distance “s” were taken to determine I_{Hcu} V_{Hpot} V_{Lpot} I_{Lcu} where I_{Hcu} and I_{Lcu} were current injection at the tips while V_{Hpot} and V_{Lpot} were voltage measured at the dedicated tips. The four points were then arranged in form of a square and current was injected and corresponding voltages obtained with their $R_{12,34}$ and $R_{14,23}$ respective resistances computed. The spacing between tip points was each varied at fixed values of 1mm to 5 mm and resistivity determined as a function of frequency, thickness and type of configuration. Five points were tested for frequency ranges from 5×10^3 Hz to 4×10^4 Hz. Two different film with thicknesses 3.3 μ m and 5.2 μ m were chosen and were tested both in aligned and in square configurations.

3.3.2 Numerical simulation

Numerical simulations were carried out using the SCAPS-1D software on the model photo cell shown in Fig. 1.

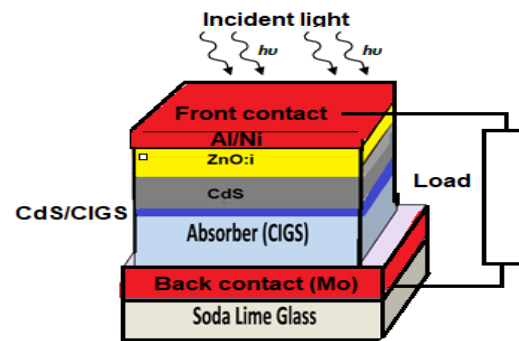


Fig. 1. CIGS model photo cell

During simulation, most parameters of the different layers were kept constant in order to determine the qualitative and quantitative relationship between bulk defect density and its electrical parameters. Bulk defect density was varied from 10^{12} cm^{-3} to 10^{18} cm^{-3} to investigate the photocell’s quantum efficiency. Some extra external parameters were added into the SCAPS-1D software help in the extraction of electrical and photo cells parameters of interest from each layers, interfaces and photocell are summarized in Table 1.

Table 1. Selected parameters used in the SCAPS-1D software to simulate the CIGS photo cell performance {D= Donor, *A= Acceptor}

Layers properties	Units	i-ZnO	CdS	CIGS
Photo cell temperature	K	300	300	300
Standard illumination spectrum	G	1.5	1.5	1.5
Doping concentration	cm^{-3}	10^{17} (D)	10^{17} (D)	10^{16} (A)
Approximate layer thickness	nm	350	60	2550
Working density of bulk defects	cm^{-3}	10^{16}	10^{16}	10^{14}
Theoretical band gap energy	eV	3.321	2.413	1.245
Effective electron affinity	eV	4.445	Variable	Variable
Effective electron mobility	cm^2/Vs	100.0	70.0	100.0
Effective electron thermal velocity	cm/s	2.41×10^7	2.43×10^7	4.19×10^7
Electron cross-section capture area	cm^2	10^{-15}	10^{-15}	Variable
External Ambient conditions	°C	15 - 35	15 - 35	15 - 35
Relative dielectric permittivity		9.03	9.81	13.56
Effective BC density of state	cm^{-3}	3.11×10^{18}	3.11×10^{18}	2.0×10^{18}
Effective BV density of state	cm^{-3}	1.8×10^{19}	3.1×10^{18}	1.5×10^{19}
Photo Constant	W/m^2	10^3	10^3	10^3
Effective thermal velocity of holes	cm/s	1.3×10^7	1.6×10^7	1.4×10^7
Effective Mobility of holes	cm^2/Vs	31.3	19.8	12.5
Hole capture cross-section area	cm^2	2.0×10^{-13}	2.0×10^{-13}	2.0×10^{-13}

4. RESULTS AND DISCUSSION

4.1 Influence of Bulk Defect Density on Resistivity

4.1.1 Influence on frequency and tip spacing

Fig. 2 to Fig. 6 represents graphical representations on the variations in frequency against resistivity. Fig. 2 specifically shows the variation of resistivity with frequency when the tip points were separated by a distance of 1mm.

As shown in Fig. 2, whenever there was a constant tip spacing in the aligned configuration, resistivity was always higher in the 5.2 μm (thick film) as compared to the 3.3 μm (thinner film). A similarly observation was seen in the square configuration. However, at the same frequency in both types of configuration a notable difference in resistivity was noticed at different magnitudes for each CIGS film thickness. This difference was attributed to influence by bulk defect density [24]. Fig. 3 shows the variation of resistivity when tip spacing was increased to 2 mm.

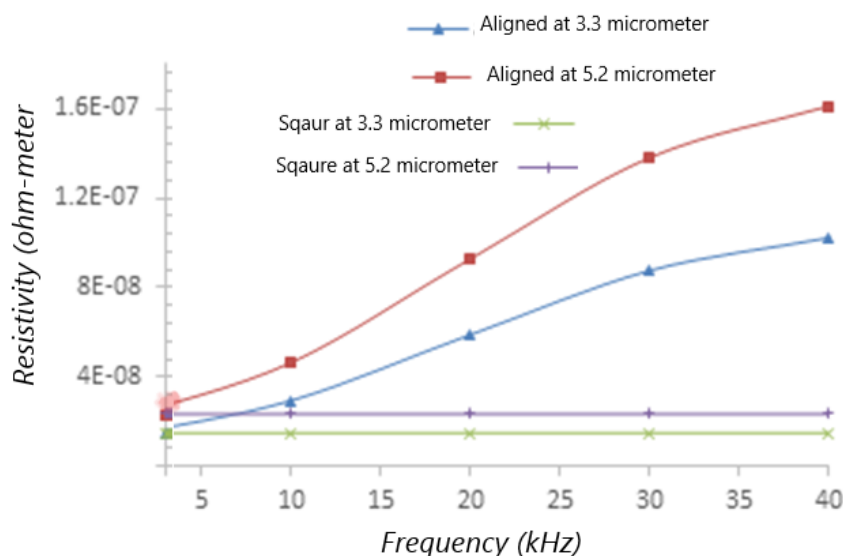


Fig. 2. Influence of frequency of 1 mm tip-spacing on resistivity

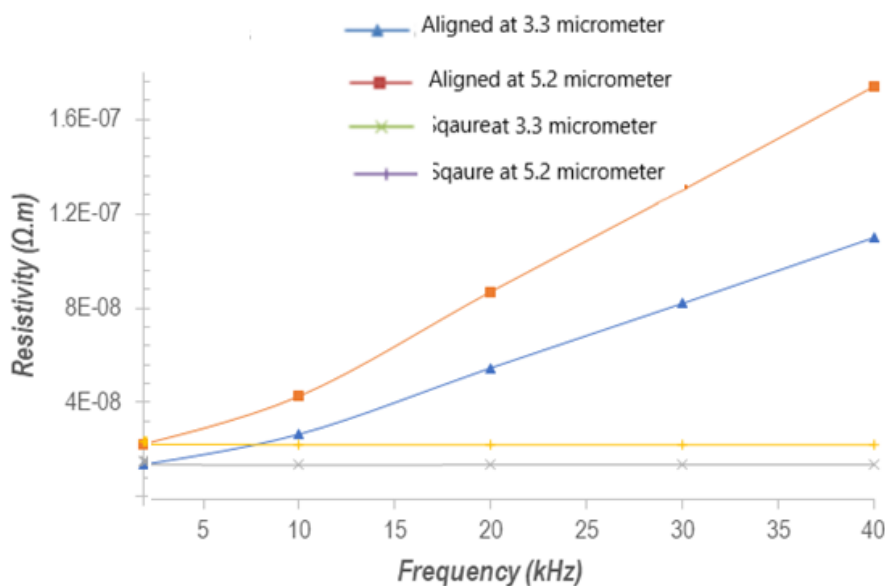


Fig. 3. Influence of frequency of 2 mm tip-spacing on resistivity

Similarly, in the aligned configuration in Fig. 3, a thicker film (5.2 μm) exhibited higher resistivity as compared to a thinner film (3.3 μm). However, in both cases, resistivity increased with frequency suggesting that frequency made contribution to resistivity. In the square configuration, the thicker film had higher resistivity as compared to a thinner film which was frequency independent. This suggested that the influence by bulk defect density on resistivity depends on the type of configuration [25], there was higher restriction to charge flow in an aligned configuration more as opposed to in the square configuration. Fig. 4 shows the relation between resistivity and frequency when tip spacing was 3 mm.

Resistivity in the square configuration remained constant with increase frequency, though the 5.2

μm film exhibited a relatively higher resistivity as compared to the 3.3 μm film. In the aligned configuration, resistivity increased as frequency increased. At 2×10^3 Hz, the resistivity of both films exhibited almost similar values that was attributed to bulk defects at resonance. These bulk defects exhibited a perfect multi-oscillator mechanism [26] that ends up transferring charge carriers from one defect to another just like the way conductors do irrespective of their thickness. Beyond the 2×10^3 Hz, the 5.2 μm film increased its resistivity sharply suggesting higher charge collisions between charges and defects behaving as charge traps or higher degree restriction centers. As a result, the resistivity for the 3 mm tip spacing were higher as compared to both the 2 mm and 1mm spacings.

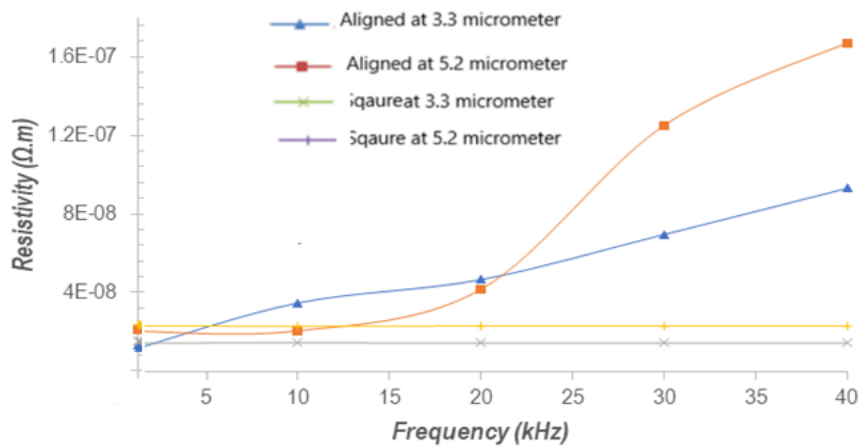


Fig. 4. Influence of frequency of 3 mm tip-spacing on resistivity

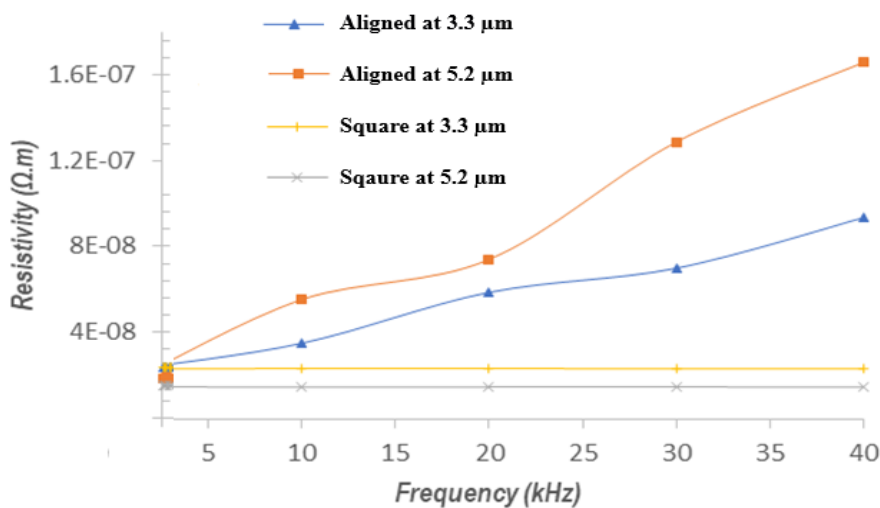


Fig. 5. Influence of frequency of 4 mm tip-spacing on resistivity

Fig. 5 shows a comparison in the variation in resistivity with frequency between the aligned configuration and square configuration when the tip spacing distance was increased to 4 mm. Resistivity was not influenced by either tip spacing nor frequency as opposed to when the tip spacing was 1mm, 2 mm and 3 mm in the square configuration while in the aligned configuration, frequency had a notable influence in resistivity of the thinner film. Resistivity in both aligned and square configurations at 2×10^3 Hz was notably very close to each other and but thereafter, the thicker film exhibited a greater increase compared to the thinner film. Fig. 6 shows how resistivity varied with frequency when the tip spacing was increased further to 5 mm.

At 5 mm tip spacing, the square configuration seemed not to be influenced by bulk defects. In the aligned configuration, a linear increase in both films was noticed at equal ratios and the influence of bulk defect density was negligible. They could not influence resistivity irrespective suggesting that there is a limit below the 5 mm tip spacing where bulk defect density can influence resistivity [27]. It can be noted that it doesn't matter how thick or how far the tip spacing is located in the square configuration, defect density does not influence resistivity. In the aligned configuration, frequency and tip spacing influence resistivity if the system is exposed to frequencies below 1000 Hz due to skin effects and proximity effects on charge flow. The abnormal resistivity levels observed above 1000 Hz should be avoided and only frequencies

below 1000 Hz should be considered when studying the influence of tip spacing in CIGS films. It was also observed that, for a tip spacing that lies below or less than 3 mm, resistivity remained constant irrespective of type of configuration and thickness as long as frequency was below 1000 Hz. Similarly, for tip spacing above 3 mm, there was resistivity inversion as a function of thickness only in the aligned configuration (*such that resistivity values for the thickest films become lower while those of the thinner film becomes higher*). This was not the same in the square configuration where resistivity remained constant for all cases when tip spacing was less than 3 mm. The inversion can only be justified by considering the limitations of the aligned configuration where injected current must be adjusted to control the measured voltage across the film so as to obtain the same sheet resistance. Therefore, resistivity is a function of the tip spacing which can be considered as a restriction when using the aligned configuration. It is necessary to limit resistivity measurements to below 1000 Hz when tip spacing is less than 3 mm so that both between aligned and square configurations can agree in their measurements.

4.1.2 Influence on tip disposition

Fig. 7 to Fig. 9 show the variation between resistivity as function tip spacing for frequencies of 50 Hz, 500 Hz and 1000 Hz in both the aligned and square configurations on $3.3 \mu\text{m}$ and $5.2 \mu\text{m}$ CIGS film thicknesses.

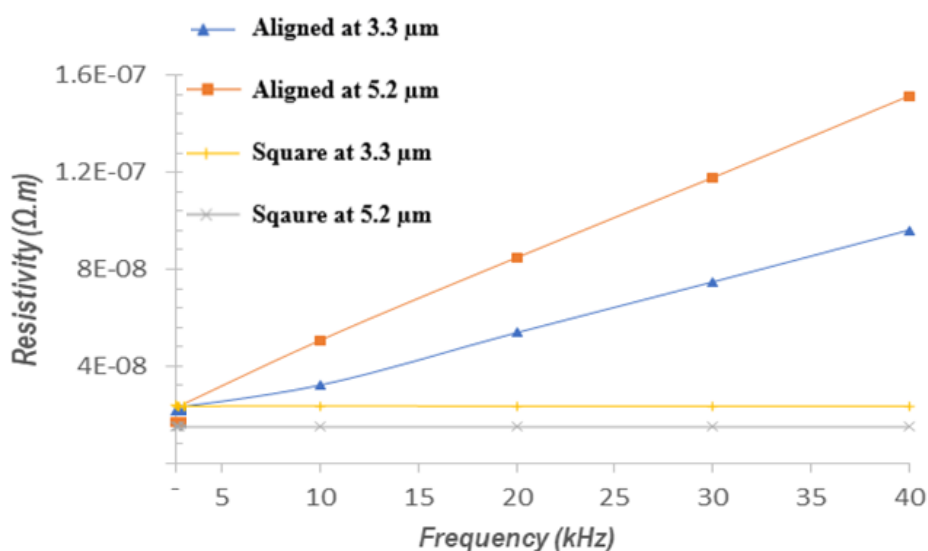


Fig. 6. Influence of frequency of 5 mm tip-spacing on resistivity

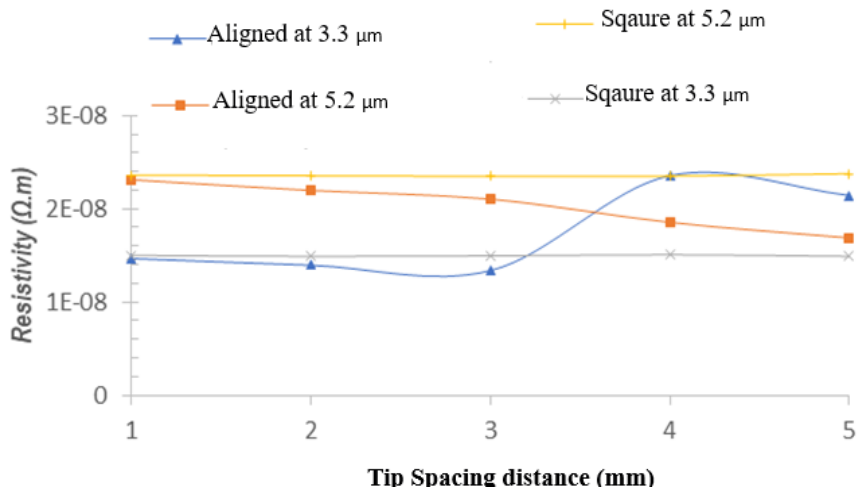


Fig. 7. Influence of tip-spacing on resistivity at 50 Hz

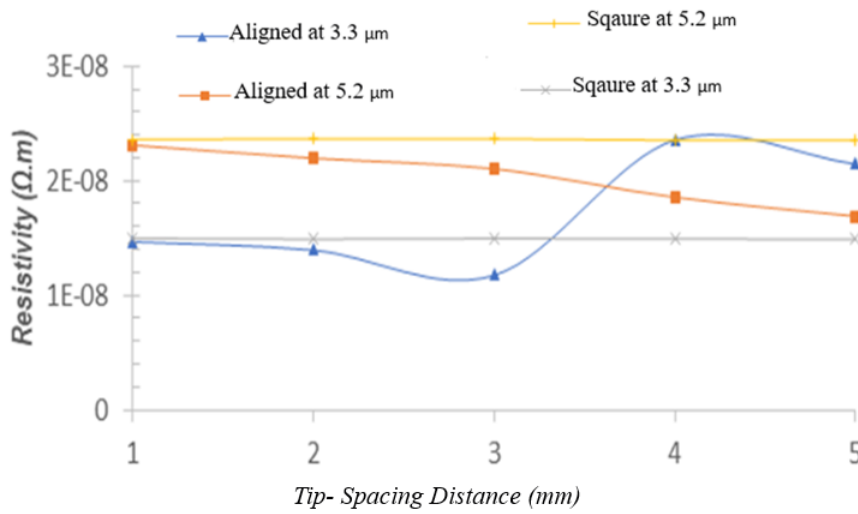


Fig. 8. Influence of tip-spacing on resistivity at 400 Hz

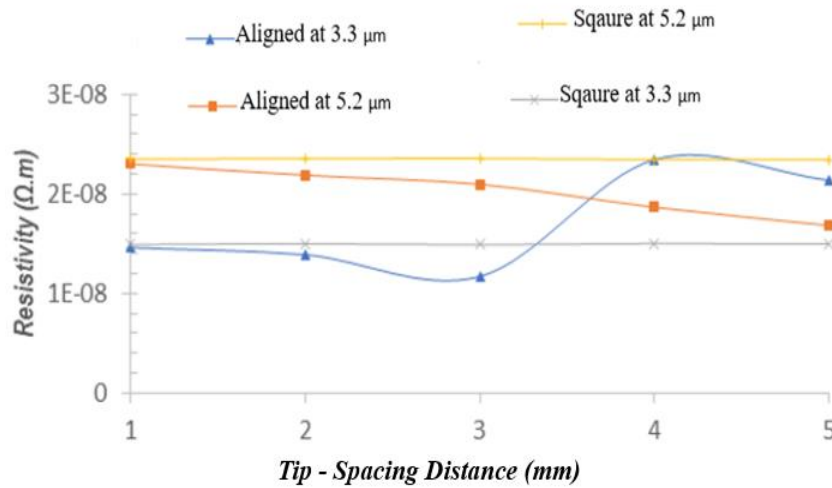


Fig. 9. Influence of tip-spacing on resistivity at 1000 Hz

Fig. 7, Fig. 8 and Fig. 9 shows a constant resistivity for both thickness and tip spacing in the square configuration with variance that followed Eq. (3). In aligned configuration, resistivity changed with changes in tip spacing and thickness by notable variations. The 3.3 μm film exhibited less resistivity than the nominal resistivity of a metallic copper solid (*which is a component in CIGS film*) but whose resistivity increased as soon as tip spacing increased above 3 mm. In the 5.2 μm film resistivity was higher than that of solid copper but decreased whenever the tip spacing was increased above 3 mm. This was a sign of an influence by an intrinsic phenomenon [28] that conforms to an aligned configuration which was suspected to be bulk defect density. To obtain a resistivity that is comparable in both configurations, the tip spacing must be limited to below 3 mm. When tip spacing was 1 mm, there was an almost perfect concordance in measurements in both configurations. In aligned configuration, the resistivity depended on spacing between tips unlike in the square configuration. A rise in temperature caused an increase in thermal vibrations [29] of atomic particles generating lattice irregularities that ended up acting as electron scattering centres [30] increasing resistivity and grain boundaries and hence becoming effective electron scattering sites. As the number of grain boundaries increases [16], resistivity also increases implying an increase in effective electron scattering sites. Bulk defects or grain boundaries provide barriers for charge dislocations [31] and transmission through thin films but they do not interfere with electrons

trespassing within the film. Table 2 illustrates the percentage variance for three selected frequencies of 50 Hz, 500 Hz and 1000 Hz for tip spacing of 2.0 mm, 3.0 mm, 4.0 mm and 5.0 mm as compared from tip spacing of 1.0 mm.

From Table 2, it can be noticed that the percentage resistivity variance values are below 10% for all tip spacing below 3 mm. This is the most acceptable variance and therefore, resistivity measurement in CIGS thin films in aligned configurations can be recommended to be done when the tip spacing is less 3.0 mm and when the frequency is below 1000 Hz. It is recommended that when designing a photocell that will use CIGS as an absorber layer, one has to consider the influence of bulk defect density as a factor influencing charge flow.

4.2 Influence of Bulk Defect Density on I-V Curve

Fig. 10 shows the I-V characteristics profile curves for different bulk defect densities in CIGS absorber layers as generated by the SCADS-1D simulation software.

By varying the bulk defect density from 10^{12} cm^{-3} to 10^{18} cm^{-3} , the fill factor, J_{sc} , efficiency, η and V_{oc} revealed three distinct zones. There was a notable reduction in photon absorption in the photocell. The profile I-V curves highlights three distinctive operational zones shown in Fig. 11 and labeled as I, II and III respectively.

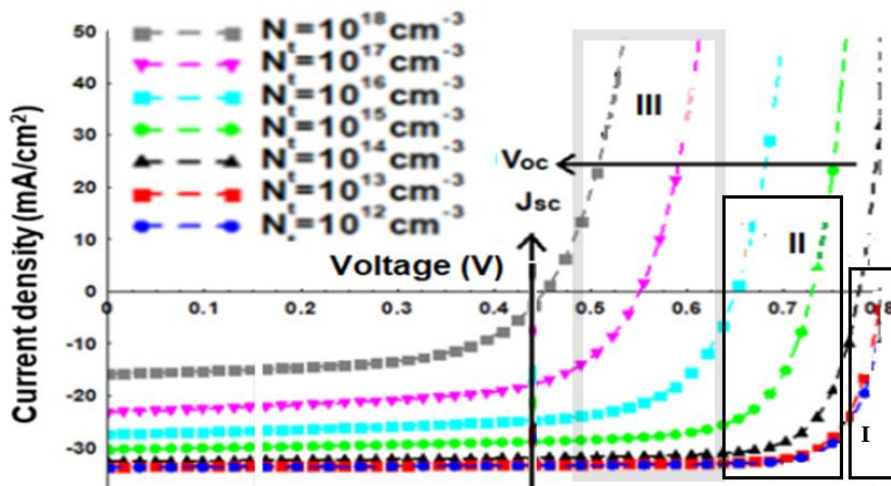


Fig. 10. I-V profile characteristics for different bulk defect densities

Table 2. Percentage variance in resistivity in aligned configuration for three selected frequencies and four tip spacing distances

Tip Spacing (mm)	3.3µm	5.2µm	3.3µm	5.2µm	3.3µm	5.2µm
Frequency (Hz)	50		500		1000	
2.0	-5.13	-5.22	-5.12	-5.20	-5.21	-5.13
3.0	-9.21	-9.18	-20.2	-9.14	-20.5	-9.17
4.0	61.11	-20.00	61.11	-20.11	61.23	-19.97
5.0	46.52	-27.13	46.45	-27.5	46.43	-27.5

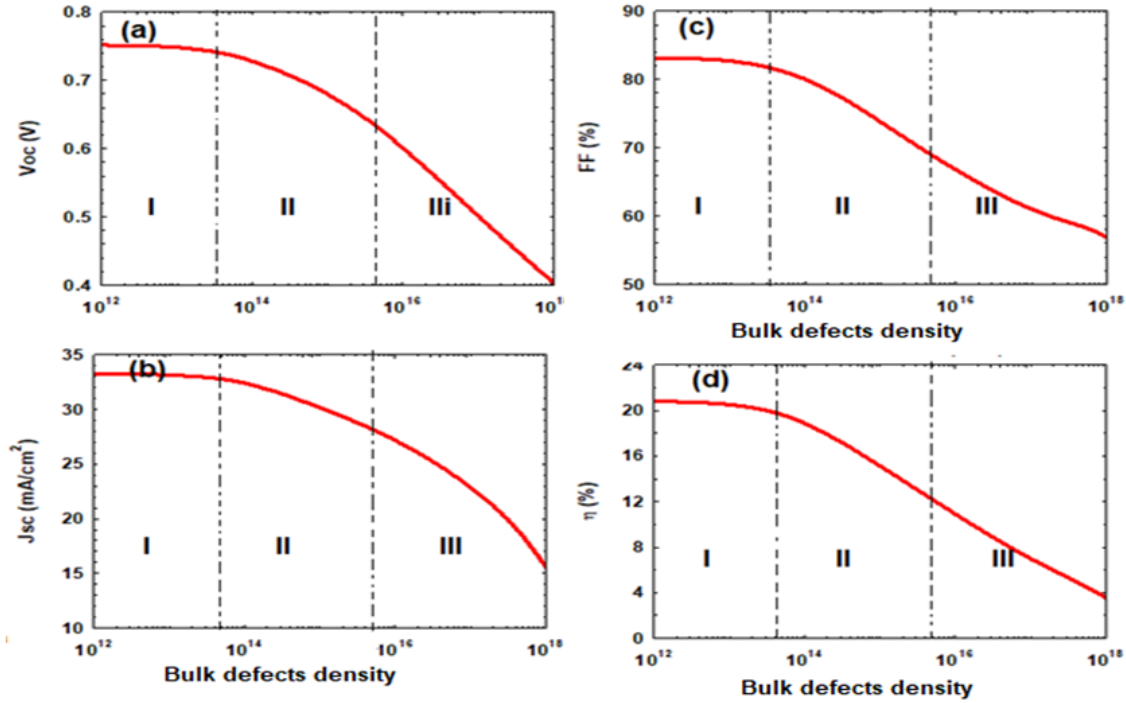


Fig. 11. Influence of bulk defect density on short circuit current, fill factor, efficiency and open circuit voltage

The bulk defect density in zone I, was less than $5 \times 10^{13} \text{ cm}^{-3}$ and had a less influence on the photocell operation and as a result, the photocell had very good and almost constant performance due to the Shockley-Read-Hall recombinations [32]. In zone II, the bulk defect density was between $5 \times 10^{13} \text{ cm}^{-3}$ and $5 \times 10^{15} \text{ cm}^{-3}$ decreased the photocell's performance. In zone III, the defect density was slightly above $5 \times 10^{15} \text{ cm}^{-3}$ where most of electrical parameters highly depend on the concentration of defects. There was an abruptly decrease in the photocell's performance. A large defect concentration decreases charge carrier lifetime [33] proportionally as:

$$\tau_n = \frac{1}{\sigma_n v_n N_t} \quad (10)$$

where τ_n is lifetime, D_n is diffusion constant, v_n is thermal velocity, N_t is bulk defect density in absorber, σ_n is capture cross-section of the film and L_n is diffusion length of the electrons. The decrease in lifetime favour recombination rates but proportionally affect their diffusion lengths by [34]:

$$L_n = \sqrt{D_n \tau_n} \quad (11)$$

Literature confirms that impurities [32, 33, 35,] and defects [36, 37] strongly influence properties of CIGS absorbers. Impurities or defects can be added to either increase conductivity or control charge carrier lifetime and recent studies reveals that defects are closely linked to film growth mechanisms in CIGS that include but are not

limited to gravitational sedimentation [37], inertial impactation [38] and Brownian diffusion [39], mixed induction by turbulent flow [40], electrostatic precipitation [41], interception [42] and in part by elongation of particles [43]. Some impurities cause imperfections in a lattice crystal and end up acting as recombination sites which explains the reduction in photon absorption by the photocell.

4.3 Influence of Bulk Defect Density on Quantum Efficiency

Fig. 12 shows the variation of quantum efficiency against wavelength for different bulk defect densities.

From Fig. 12, there is a very high quantum yield in zone I suggesting an almost 100% photon absorption which explains the quality electrical features in zone I. In zone II, photon absorption decreased reducing the photo cell performance due to recombinations per unit volume space as compared to zone III where there is a drastic decrease photon absorption. The three operating zones establishes a quality link to the CIGS absorber layer suggesting that thickness, bandgap and doping concentration are influenced by bulk defect density. Therefore, defects in CIGS have a significant impact on the performance of CIGS photocell.

4.4 Influence Bulk Defect Density on Thickness

Fig. 13 illustrates the influence of bulk defect density in CIGS on fill factor, short circuit current, open circuit voltage and photocell efficiency at different thicknesses.

In Fig. 13, the short circuit current, fill factor, photo cell efficiency and open circuit voltage are affected by thickness in Zone I, II and zone III. When the thicknesses was between 0.6 μm and 2.7 μm , these parameters decrease slightly. They were almost insensitive to variation in thickness but highly depended defect density. Below 0.5 μm , there was a drastic decrease due to incomplete photon absorption by the thinner absorber layer [10] attributed to the closer proximity towards the front surface of the absorber and the rear contact [10] that increase recombinations. There was also a decreased photon absorption near the rear contact at short-wavelengths. The rear contact is a region where we have the highest recombination rates [20]. In zone I, short circuit current, fill factor, photo cell efficiency and open circuit voltage are significantly better as compared to Zone II and Zone III respectively due to reduced recombinations that can be attributed to low bulk defect density [44,45] in CIGS layer which leads to a longer lifetimes of photo-generated charge carriers. Zone I is the only zone with optimal performance.

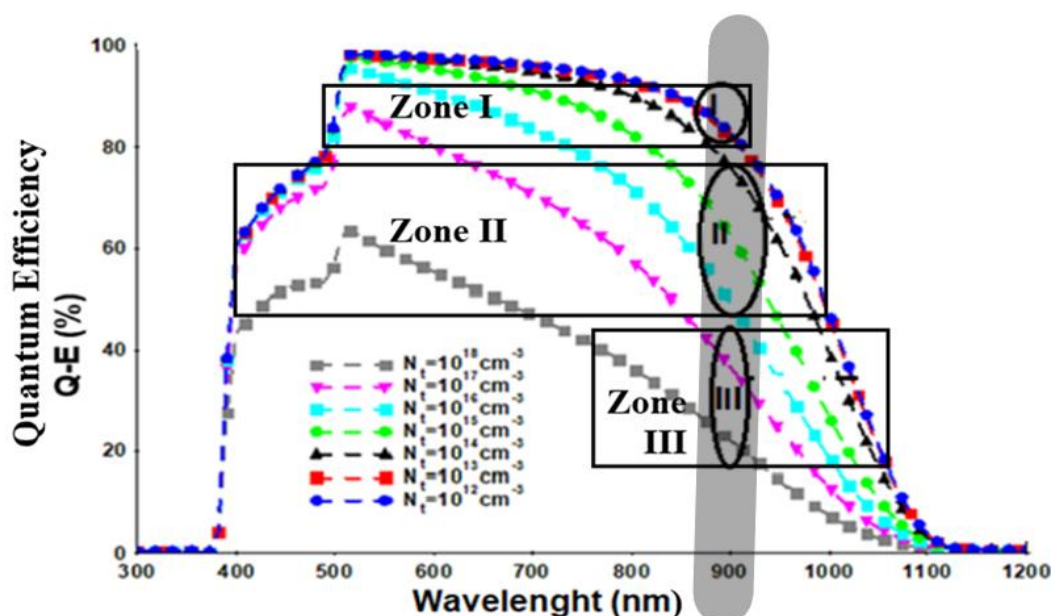


Fig. 12. Quantum efficiency for different bulk defects

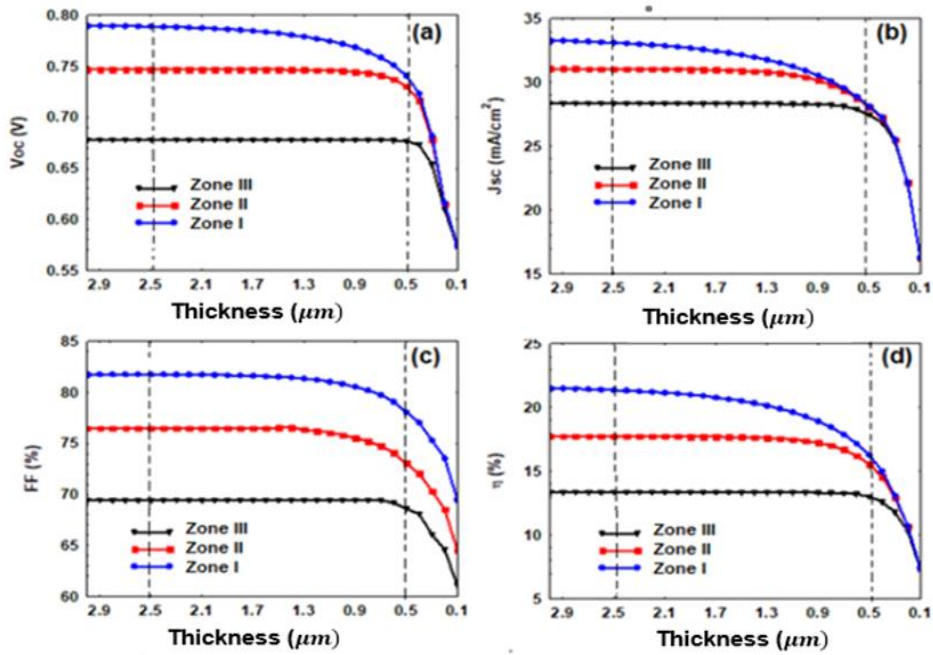


Fig. 13. Influence of CIGS layer on thickness and short circuit current, fill factor, efficiency and open circuit voltage

4.5 Influence of Bulk Defect Density on Band Gap Energy

Fig. 14 illustrates the influence of bulk defect density on band gap for different electrical parameters showing a correlation between defect density and bandgap.

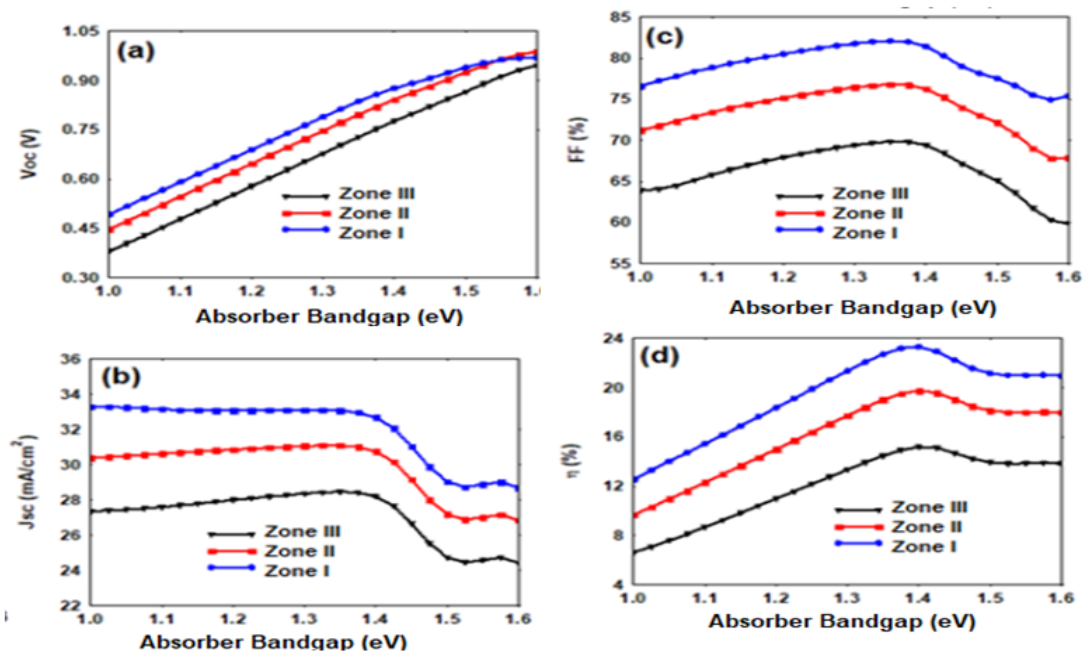


Fig. 14. Influence of bulk defect on band gap on the on short circuit current density, fill factor, open circuit voltage and photo cell efficiency

In Fig.14, J_{sc} , FF, V_{oc} and η depend on bulk defect density which influences band gap. Open-circuit voltage increased linearly whenever band gap was less than 1.412 eV in fig. 14 (a)) and vice versa in agreement with absorption coefficient α relationship given as [9] :

$$\alpha = \frac{B}{h\gamma} (h\gamma - E_g)^{\frac{1}{2}} \quad (12)$$

where h is the Planck constant while γ is wave frequency. Increasing the concentration of Ga in CIGS films reduced regeneration rate at the $P-N$ junction [45] and thus, fill factor and efficiency exhibited almost the same trend increasing band gap to have its optimal performance when it lies between 1.31 eV and 1.42 eV to produce a corresponding efficiency of between 0.45 and 0.61 respectively.

4.6 Influence of Bulk Defect Density on Acceptor Density

Fig. 15 illustrates how bulk defect density influence short circuit current density, fill factor,

open circuit voltage and efficiency in CIGS photocells.

From Fig. 15 (a)-(d), all the cell parameters were independent of acceptor densities below 10^{13} cm^{-3} while when it was greater than 10^{13} cm^{-3} , open circuit voltage increased. For every excessive acceptor density above 10^{16} cm^{-3} , open circuit voltage decreased significantly. Similarly, short-circuit current density became almost insensitive for acceptor densities below 10^{14} cm^{-3} but decreased whenever acceptor concentration exceeded 10^{14} cm^{-3} . A similarly trend was observed for conversion efficiency and fill factor in line with Fig. 5 in Zone I and Zone II respectively. Bulk defect density determined the quality (*defect free*) of the CIGS absorber layer. Therefore, by controlling doping, you control the density of bulk defects or you control the quantity of acceptors, charge carrier mobility and lifetimes [12] available which affect photo cell performance. Doping has been linked to the presence of intrinsic defects [6, 9, 17, 46] in thin films and one study revealed that an excess of selenium introduces a n-type [46] conductivity while a deficiency of selenium lead to p-type [41]. Therefore, acceptor density is a key parameter to consider in addition to bulk defect density.

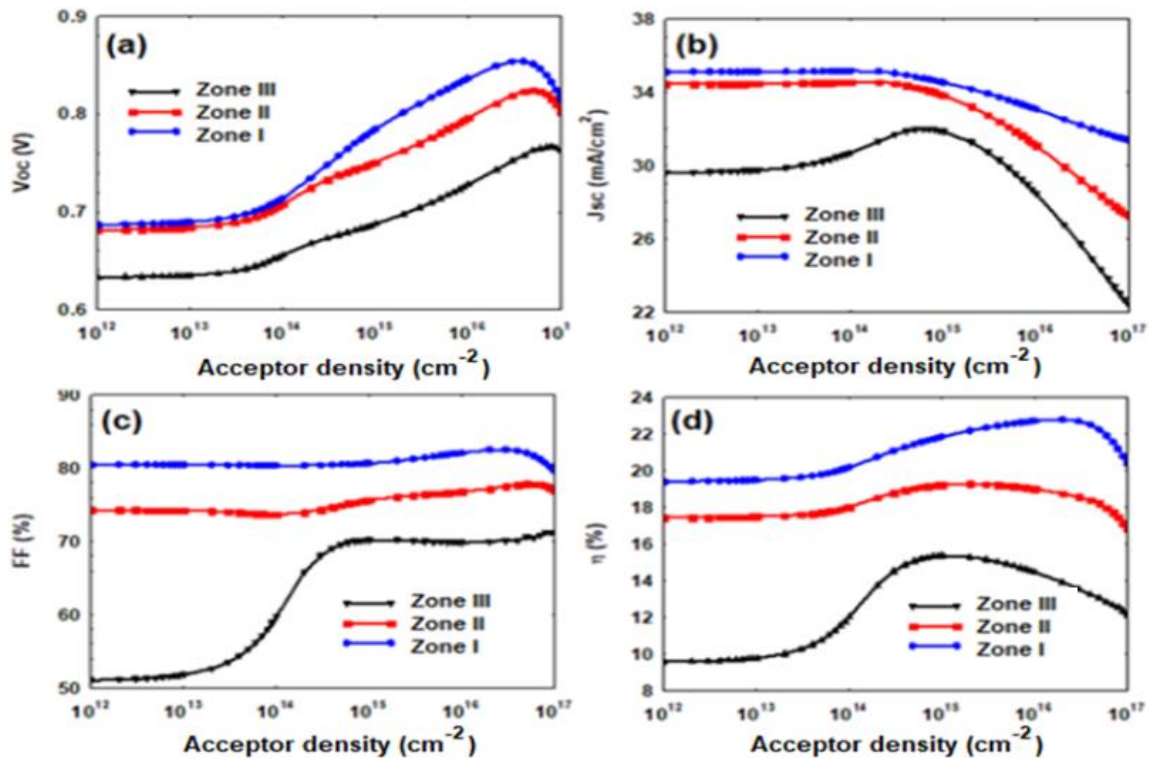


Fig. 15. Influence of bulk defects on short circuit current density, fill factor, open circuit voltage and efficiency

5. CONCLUSION

CIGS thin films are commonly used to manufacture photocells and solar cells. A study was carried out on the influence of bulk defect density in CIGS thin films. Resistivity measurements were experimentally performed using the aligned and square configurations. The findings revealed that a square configuration is more accurate as compared to aligned configuration. It enables quality measurements up to and over 40 kHz in frequency without being affected by tip spacing distances. However, when using aligned configuration, well-defined conditions must be put in place first for more accurate results. The second section of the study involved using the SCAPS-1D software to simulate the influence of bulk defect density on electrical parameters and photocell performance. Results identified three photocell operating zones that were influenced by bulk defect densities revealing that CIGS films had optimal performance when its bulk defects density was lower than $5 \times 10^{13} \text{ cm}^{-3}$ at 1.31 eV - 1.42 eV band gap energy. It was concluded that bulk defect density plays a significant role in CIGS thin films when used as an absorber layer for photon sensing application.

COMPETING INTERESTS

Author has declared that no competing interests exist.

REFERENCES

1. Li X, Ma B, Wang C, Hu D, Lü Y, Chen Y. Recycling and recovery of spent copper—indium—gallium—diselenide (CIGS) solar cells: a review. *Int J Miner Metall Mater.* 2023;30(6):989-1002.
2. Xu X, Qu Y, Campbell S, Le Garrec M, Ford B, Barrioz V et al. Solution processing route to Na incorporation in CZTSSe nanoparticle ink solar cells on foil substrate. *J Mater Sci Mater Electron.* 2019;30(8):7883-9.
3. Lucaßen J, Sedaghat S, Schmid M. Realistic multidimensional optoelectrical modeling guide for copper indium gallium diselenide solar cells. *Sol RRL.* 2023;7(4):2200867.
4. Liu Y, Li Y, Tang J, Zhang W, Lin B, Cao Y. Efficiency enhancement of copper indium gallium selenide solar cells fabricated on polyimide foils with multiple metal layers. *Thin Solid Films.* 2023; 767:139687.
5. Jehl Z, Bouttemy M, Lincot D, Guillemoles JF, Gerard I, Etcheberry A et al. Insights on the influence of surface roughness on photovoltaic properties of state of the art copper indium gallium diselenide thin films solar cells. *J Appl Phys.* 2012;111(11).
6. Chen J, Chang X, Guo J, Gao Q, Zhang X, Liu C, Chen J. Organic Passivation of Deep Defects in Cu (In, Ga) Se₂ Film for Geometry-Simplified Compound Solar Cells. *Research.* 2023;6:0084.
7. Li X, Ma B, Wang C, Hu D, Lü Y, Chen Y. Recycling and recovery of spent copper—indium—gallium—diselenide (CIGS) solar cells: a review. *Int J Miner Metall Mater.* 2023;30(6):989-1002.
8. Hetzer MJ, Strzhemechny YM, Gao M, Contreras MA, Zunger A, Brillson LJ. Direct observation of copper depletion and potential changes at copper indium gallium diselenide grain boundaries. *Appl Phys Lett.* 2005;86(16).
9. Shin DS, Kim TH, Rah JE, Lee SB, Lim YK, Jeong J et al. Flexible real-time skin dosimeter based on a thin-film copper indium gallium selenide solar cell for electron radiation therapy. *Med Phys.* 2023;50(4):2402-16.
10. Rahman MF, Mahmud N, Alam I, Ali MH, Moon MMA, Kuddus A et al. Design and numerical analysis of CIGS-based solar cell with V₂O₅ as the BSF layer to enhance photovoltaic performance. *AIP Adv.* 2023;13(4).
11. Tan JH, Anderson WA. Current transport in copper indium gallium diselenide solar cells comparing mesa diodes to the full cell. *Sol Energy Mater Sol Cells.* 2003;77(3):283-92.
12. Mostaque SK, Mondal BK, Hossain J. Simulation approach to reach the SQ limit in CIGS-based dual-heterojunction solar cell. *Optik.* 2022;249:168278.
13. Saha B, Mondal BK, Mostaque SK, Hossain M, Hossain J. Numerical modeling of CuSbSe₂-based dual-heterojunction thin film solar cell with CGS back surface layer. *AIP Adv.* 2023;13(2).
14. Yadav V, Pandey R, Madan J. Optimizing Sb₂S₃ Photovoltaic Performance through Minimization of Bulk and Interface Defects. In *2023 International Conference on Sustainable Computing and Data Communication Systems (ICSCDS)*. IEEE. 2023;990-993.
15. Deo M, Chauhan RK. Tweaking the performance of thin film CIGS solar cell

- using InP as buffer layer. *Optik*. 2023;273:170357.
16. Wang R, Qin D, Zheng S, Weng G, Hu X, Tao J et al. Influence of S-content ratios on the defect properties of Sb₂(S_x, Se_{1-x})₃ thin-film solar cells. *Sol Energy Mater Sol Cells*. 2023;260:112501.
 17. Yilmaz P, de Wild J, Aninat R, Weber T, Vermang B, Schmitz J et al. In-depth analysis of potential-induced degradation in a commercial CIGS PV module. *Prog Photovolt Res Appl*. 2023;31(6):627-36.
 18. Singh AK, Chauhan MS, Patel SP, Singh RS, Singh VK. MAPbI₃-on-CuInSe₂ two-terminal monolithically integrated and four-terminal mechanically stacked tandem solar cells: A Theoretical Investigation Using SCAPS-1D. *Results Opt*. 2023;10:100358.
 19. Kumar S, Chauhan RK. Performance up-gradation of CIGS solar cell using Ag₂S quantum dot as buffer layer. *J Mater Res*. 2023;38(10):2689-700.
 20. Sultana SM, Hasan M, Ferdous MJ, Tisha IJK, Nayan MF. Defect density dependent performance analysis of perovskite solar cell for different electron transport layers. *J Optoelectron Commun*. 2023;5(1):1-10.
 21. Chen J, Chang X, Guo J, Gao Q, Zhang X, Liu C, Chen J. Organic Passivation of Deep Defects in Cu(In, Ga)Se₂ Film for Geometry-Simplified Compound Solar Cells. *Research*. 2023;6:0084.
 22. Chee AKW. On current technology for light absorber materials used in highly efficient industrial solar cells. *Renew Sustain Energy Rev*. 2023;173:113027.
 23. Khac DL, Chowdhury S, Luengchavanon M, Jamal MS, Laref A, Techato K et al. Influence/effect of deep-level defect of absorber layer and n/l interface on the performance of antimony triselenide solar cells by numerical simulation. *Sustainability*. 2022;14(11):6780.
 24. Lin J, Chen G, Ahmad N, Ishaq M, Chen S, Su Z et al. Back contact interfacial modification mechanism in highly-efficient antimony selenide thin-film solar cells. *J Energy Chem*. 2023;80:256-64.
 25. Ahmad F, Civiletti BJ, Monk PB, Lakhtakia A. Effects of defect density, minority carrier lifetime, doping density, and absorber-layer thickness in CIGS and CZTSSe thin-film solar cells. *Journal of Photonics for Energy*. 2023;13(2):025502-025502.
 26. Yadav RK, Pawar PS, Nandi R, Neerugatti KE, Kim YT, Cho JY et al. A qualitative study of SnSe thin film solar cells using SCAPS 1D and comparison with experimental results: a pathway towards 22.69% efficiency. *Sol Energy Mater Sol Cells*. 2022;244:111835.
 27. Huang ZP, Chen YX, Huang ZH, Lin WW, Mao Y, Lin LM et al. Simulation of highly efficient GeSe-based solar cells with SCAPS-1D. *Heliyon*. 2023;9(8):e18776.
 28. Cheragee SH, Alam MJ. Device modeling and numerical study of a double absorber solar cell using a variety of electron transport materials. *Heliyon*. 2023;9(7):e18265.
 29. Kumar R, Kumar A. Performance enhancement of ZnMgO:Al/ZnMgO/CIGSSe solar cell with the combination of CZTGS₂ HT-ERL layer. *J Electron Mater*. 2022;51(1):84-103.
 30. Li TC, Chang CW, Tai CC, Ho JJ, Hsieh TP, Liu YT, Lu TL. Optoelectronic Effects of Copper-Indium-Gallium-Sulfur (CIGS₂)-Solar Cells prepared by Three-stage Co-evaporation Process Technology; 2023.
 31. Rana AD, Pharne ID, Bhargava K. Numerical simulation of highly efficient double perovskite solar cell using SCAPS-1D. *Mater Today Proc*. 2023;73:584-9.
 32. Deo M, Chauhan RK, Kumar M. Optimization and performance enhancement of InP/CIGS/CuI solar cell using bandgap grading. *J Opt*. 2023;1-11.
 33. Ghorashi SMB, Karimi P, Jahantigh F, Esmaeili-Zare M. Optical simulation and investigation of different coating methods CdS&TiO₂ for buffer layer in CIGS solar cell efficiency. *Appl Phys A*. 2022;128(5):402.
 34. Hosen A, Ahmed SRA. Performance analysis of SnS solar cell with a hole transport layer based on experimentally extracted device parameters. *J Alloys Compd*. 2022;909:164823.
 35. Das MK, Panda S, Mohapatra N. Power conversion efficiency optimization of LaFeO₃ Mott insulator based solar cell with metal oxide transport layers using SCAPS. *Mater Today Proc*. 2023;74:756-62.
 36. Ali MH, Al Mamun MA, Haque MD, Rahman MF, Hossain MK, Md Touhidul Islam AZ. Performance enhancement of an MoS₂-based heterojunction solar cell with an In₂Te₃ back surface field: A numerical simulation approach. *ACS Omega*. 2023;8(7):7017-29.

37. Zein W, Alanazi TI, Salah MM, Saeed A. Concurrent design of alloy compositions of CZTSSe and CdZnS using SCAPS simulation: potential routes to overcoming VOC deficit. *Energies*. 2023;16(15):5754.
38. Bhattarai S, Hossain MK, Pandey R, Madan J, Samajdar DP, Rahman MF et al. Perovskite solar cells with dual light absorber layers for performance efficiency exceeding 30%. *Energy Fuels*. 2023;37(14):10631-41.
39. Wang S, Li MH, Zhang Y, Jiang Y, Xu L, Wang F, Hu JS. Surface n-type band bending for stable inverted CsPbI₃ perovskite solar cells with over 20% efficiency. *Energy & Environmental Science*; 2023.
40. Kanchan K, Sahu A, Kumar B. Numerical Simulation of Copper Indium Gallium Diselenide Solar Cell with Ultra-Thin BaSi₂ Back Surface Field Layer Using the Non-Toxic In₂Se₃ Buffer Layer. *Silicon*. 2022;14(18):12675-12682.
41. Bhatnagar A, Srivastava S, Janyani V. Design and performance investigation of a highly efficient copper-indium-gallium-selenide solar cell. *Journal of Nanophotonics*. 2021;15(3):036006-036006
42. Lawani CO, Ibeha GJ, Ige O, Danladi E, Emmanuela JO, Ukwanya AJ, Oyedare PO. Numerical Simulation of Copper Indium Gallium Diselenide Solar Cells Using One Dimensional SCAPS Software. *Journal of the Nigerian Society of physical Sciences*. 2021;48-58.
43. Farooq W, Alshahrani T, Kazmi SAA, Iqbal J, Khan HA, Khan M et al. Materials optimization for thin-film copper indium gallium selenide (CIGS) solar cell based on distributed Bragg reflector. *Optik*. 2021;227:165987.
44. Sultana MR, Islam B, Ahmed SRA. Modeling and performance analysis of highly efficient copper indium gallium selenide solar cell with Cu₂O hole transport layer using solar cell capacitance simulator in one dimension. *Physica Status Solidi (a)*. 2022; 219(5):2100512.
45. Nwakanma O, Velumani S, Morales-Acevedo A. Review on the effects due to alkali metals on copper—indium—gallium—selenide solar cells. *Mater Today Energy*. 2021;20:100617.
46. Saeed M, González Peña OI. Mass transfer study on improved chemistry for electrodeposition of copper indium gallium selenide (CIGS) compound for photovoltaics applications. *Nanomaterials (Basel)*. 2021;11(5):1222.